Resonance states in a cylindrical quantum dot with an external magnetic field

Alba Y Ramos and Omar Osenda

Facultad de Matemática, Astronomía y Física, Universidad Nacional de Córdoba, Córdoba, Argentina and IFEG-CONICET, Ciudad Universitaria, X5016LAE Córdoba, Argentina

Abstract. Bound and resonance states of quantum dots play a significant role in photo-absorption processes. In this work, we analyze a cylindrical quantum dot, its spectrum and, in particular, the behaviour of the lowest resonance state when a magnetic field is applied along the symmetry axis of the cylinder. To obtain the energy and width of the resonance we use the complex rotation method. As it is expected the structure of the spectrum is strongly influenced by the Landau levels associated to the magnetic field. We show how this structure affects the behaviour of the resonance state and that the binding of the resonance has a clear interpretation in terms of the Landau levels and the probability of localization of the resonance state. The localization probability and the fidelity of the lowest energy state allow to identify two different physical regimes, a large field-small quantum dot radius regime and a small field-large quantum dot radius, where the binding of the resonance is dominated by the field strength or the potential well, respectively.

PACS numbers: 73.22.-f,31.15.-p

1. Introduction

The availability of quantum devices with characteristic length of only a few nanometer allows the implementation of a number of experimental setups that put under test the very foundations of Quantum Mechanics. The fact that the radius of a Landau level is of only a few nanometers for magnetic field strengths of around 10 Tesla allows the verification of the Aharonov-Bohm effect in quantum rings [1], which leads to the presence of persistent currents [2]. This persistent currents have been measured even for one electron states [3]. The quantum rings are formed by only one semiconductor material, and the fabrication of multiple concentric quantum rings (up to five) can be achieved with high quality and reliability [4].

The early realization that the quantum dots presented an ideal scenario to study transitions between electrically confined states and Landau-type magnetic levels [5], originated numerous theoretical and experimental works attempting to explain the effect of the confinement potential over the observed spectrum. For example, Peeters and collaborators studied the spectral properties of two-dimensional parabolic confinement potential [6], the effect of the confinement in the direction of the field (or z direction) [7, 8], and the spectral properties of a electron confined in an artificial molecule [9]. Anyway, even in the case of a finite confinement potential in the z direction [8], these studies were restricted to the discrete spectrum of each problem.

On the other hand, the quantum dot has been appointed as one of the most promising implementations of a single qubit [10, 11]. There has been a huge amount of work to circumvent the numerous associated problems: decoherence [12], the coupling between two qubits (to implement a two-qubit quantum gate) in double quantum dots has been studied extensively, in particular how it can be tuned using electric fields [13], magnetic fields [14], or the effect of the confinement of the double quantum dot in a quantum wire [15], etc.

When dealing with applied magnetic fields, most theoretical studies on quantum dots focus on strongly localized states, many times achieved using always-bounding potentials, as the three dimensional harmonic potential or impenetrable walls. The presence of a constant magnetic field, anyway, is equivalent to a two dimensional harmonic potential in the plane orthogonal to the field direction. Conversely, there are far less examples of studies considering finite potentials, in particular those whose shapes or features allow the presence of resonance states. There is a number of reason to study finite potentials, from charge transport situations to the effect of resonance states in luminescent quantum dots. Bylicki and Jaskólski [16] analyzed the binding of shape resonances through the application of an external magnetic field. They considered an one-electron spherical quantum dot-quantum well structure (QDQW). In this work we consider a closely related problem with the purpose of a better understanding of the transition from a resonance state to a bounded one.

As has been said above, a constant magnetic field induces a two-dimensional harmonic potential that precludes the appearance of resonances in the plane orthogonal

to the field, *i.e.* the loss of particles can take place **only** in the direction of the field, closing a number of decaying channels that would be available in absence of the field. In this sense, it renders almost irrelevant what particular shape has the binding potential, as long as it allows the appearance of resonances in the direction of the field. So, to avoid unnecessary complications, we consider a quantum dot model with cylindrical symmetry whose axis has the same direction that the magnetic field, besides we use the Effective Mass Approximation (EMA). As it is well known in this approximation the many-body interactions of the electron trapped in the quantum dot are reduced to a (simple) bounding potential, and all the parameters of the Hamiltonian, mass, dielectric constants, and so on are taken as equal to the the bulk parameters.

Despite its apparent simplicity, the calculation of the resonance states of one electron trapped in a bounding potential with an external magnetic field is far from trivial, in particular for small enough strengths of the field since the Landau levels are bunched when the strength of the field goes to zero. To obtain the energy and width of the resonance states we employ the complex scaling method [17] that, together with a square-integrable variational approximation for the wave function, has been used to analyze the bound and resonance states of two electron quantum dots [18]. Moreover, as has been shown in [18], the fidelity of the variational eigenstates is a good tool to detect the resonance states. In this work we use the fidelity to study the binding of a resonance and show that it is signaled by a sharp change in the behavior of the fidelity. This feature is consistent with the behavior observed in the fidelity when the system experiments a quantum phase transition (in many-body models), is near the ionization threshold or to a resonance [18]. Recently, the application of concepts from Quantum Information Theory, as the fidelity or entanglement, has been very fruitful to analyze bound and resonance states in few body systems as two-electron quantum dots [18, 19, 20, 21], or two-electron He-like systems [22, 23].

The paper is organized as follows, the quantum dot model and the variational approximation that provides approximate eigenvalues and eigenfunctions are presented in Section 2. The analysis of the resonance using complex exterior scaling and the influence of the Landau levels are presented in Section 3 , while the binding process is studied, using different methods, in Sections 3,4 and 5. Finally, we summarize and discuss our results in Section 6. Some rather lengthly and technical results, mostly matrix elements are deferred to the Appendices

2. Model

The bounding potential of the quantum dot is given by a piecewise function

$$V(\rho,z)=\begin{cases} V_1, & \rho<a_\rho,\ \frac{a_z}{2}<|z|<\frac{a_z+b_z}{2} \\ -V_2, & \rho<a_\rho,\ |z|<\frac{a_z}{2} \\ 0, & \rho\geq a_\rho,\ |z|\geq\frac{a_z+b_z}{2} \end{cases} \tag{1}$$

i.e. the potential is a cylindrical well aligned with the z-axis, with two potential steps at the top and the bottom of the cylinder, where the radius of the cylinder is a_ρ, its

height a_z, the depth of the potential well, $-V_2$, and the height of the potential steps, V_1. This ensures that, for properly chosen constants a_z, b_z, a_ρ, V_1 and V_2 the one electron problem has resonance states without external field.

Even with the introduction of the external field the angular momentum L_z is a conserved quantity, and its eigenvalues good quantum numbers. So, we focus on states with zero angular momentum L_z. In this case, the Hamiltonian reads as

$$H_0 = -\frac{1}{2\mu}\left(\frac{1}{\rho}\frac{\partial}{\partial\rho}\left(\rho\frac{\partial}{\partial\rho}\right) + \frac{\partial^2}{\partial z^2}\right) + V(\rho, z) \tag{2}$$

where $V(\rho, z)$ is given by Equation 1, μ is the effective mass of the electron in the semiconductor material. The Equation is written in atomic units. If a magnetic field $\mathbf{B} = B\hat{\mathbf{z}}$ is applied, there is a new term that must be incorporated to the RHS of Equation 2, which results in the following Hamiltonian [16]

$$H = H_0 + \frac{B^2}{8\mu}\rho^2. \tag{3}$$

The discrete spectrum and the resonance states of the model given by Eq. (3) can be obtained approximately using square-integrable variational functions Ψ_j^v [18, 19, 24, 25]. So, if Ψ_j are the exact eigenfunctions of the Hamiltonian, we look for variational approximations

$$\Psi_j \simeq \Psi_j^v = \sum_{i=1}^{N} c_i^{(j)}\Phi_i\,, \quad c_i^{(j)} = (\mathbf{c}^{(j)})_i \qquad , j = 1, \cdots, N\,, \tag{4}$$

where the Φ_i must be chosen adequately, N is the basis set size, and the $(\mathbf{c}^{(j)})_i$ are the linear variational parameters of the Rayleigh-Ritz method.

Since we are interested in null angular momentum eigenfunctions, and taking into account the symmetries of the Hamiltonian 3, we choose as basis functions

$$\Phi_i(\rho, z) = \psi_n(\eta\rho)\phi_t(\nu z), \tag{5}$$

where

$$\psi_n(\eta\rho) = \frac{1}{\sqrt{n+1}}\eta e^{-\eta\rho/2}L_n^{(1)}\left(\eta\rho\right), \tag{6}$$

and

$$\phi_t(\nu z) = \sqrt{\frac{\nu}{2}}e^{-\nu|z|/2}L_t^{(0)}\left(\nu|z|\right), \tag{7}$$

η and ν are the non-linear variational parameters, $L_n^{(1)}$ and $L_t^{(0)}$ are associated Laguerre polynomials. As has been analyzed in previous works [18, 19], when dealing with resonance states it is convenient to choose small values for the non-linear variational parameters. In particular, along this work we use $\eta = \nu = 0.01$. If $\psi_n(\eta\rho)$, where $n = 1, \ldots, N_\rho$, and $\phi_t(\nu z)$, where $t = 1, \ldots, N_z$, then $N = N_z N_\rho$.

The matrix elements of the kinetic energy, the bounding potential and the magnetic field term are given in the Appendix. With all these matrix elements we get a variational eigenvalue problem

$$\tilde{\mathbf{H}}\mathbf{c}^{(j)} = E_j^v\mathbf{c}^{(j)}, \tag{8}$$

where the entries of the matrix $\tilde{\mathbf{H}}$ are given by

$$\tilde{\mathbf{H}}_{n,t,s,m} = \langle \psi_n \phi_t | H | \psi_s \phi_m \rangle \tag{9}$$

The ample range of materials and structures available to design self-assembled quantum dots precludes the possibility of a very general analysis, however, in part for comparison reasons, we use similar parameters than those used by Bylicki in [26] and Bylicki and Jaskólski in [16] to model a quantum dot quantum well structure made of gallium arsenide (GaAs) composites, *i.e.* $a_\rho = a_z = 7nm$, $b_z = 2.5nm$, $V_1 = 0.37eV$, $V_2 = 0.108844eV$, and $\mu = 0.041m_0$. The potential well depth is slightly different from the value used by Bylicki, but should be chosen so owed to the cylindrical symmetry employed in this work, conversely to the spherical one used by Bylicki. As we will show, this set of parameters is consistent with a resonance energy around $20meV$ with $B = 0$.

Figure 1 shows the variational eigenvalues and the exact LL as functions of the magnetic field strength B. The spectrum in Figure 1 was obtained using a basis set size $N_z = N_\rho = 50$. As can be appreciated, the eigenvalues are grouped in sets that are bounded between Landau levels given by $E_{\mathrm{LL}}(M, n) = \frac{B}{\mu}(|M| + n + 1/2)$, where M is the azimuthal angular momentum (in our case $M = 0$), and $n = 0, 1, 2, \ldots$. A pair of Landau levels delimits a region of the (B, E) plane, in this zone the eigenvalues are parallel to the lower Landau level, except for the appearance of avoided crossings. This particular feature is shown in Figure 1 b).

As can be seen very clearly from Figure 1d), the variational eigenvalues have the tendency to accumulate above the Landau levels. This feature is similar to the eigenvalue accumulation observed above the continuum threshold of a two-electron quantum dot [7, 19]. When a magnetic field is applied, each Landau level works as the bottom of a continuum. Another salient feature of the spectrum appears for large enough magnetic fields: one isolated eigenvalue with lower energy than the lowest Landau level. From a physical point of view, the origin of this state can be understood as follows: for intermediate values of the magnetic fields the wave function of the electron looks like an harmonic oscillator wave function in the (ρ, ϕ) plane and as a free particle in the z direction. The spatial extent of the wave function on the plane is roughly equivalent to the radius of a Landau level, that is larger than the radius (in the plane) of the quantum dot. When the strength of the magnetic field is increased the radius of the lowest Landau level becomes smaller and smaller reaching, at some point, a size similar to the radius of the quantum dot, at this point the state becomes localized. As we will show, the mechanism of localization can be quantified and strongly influences the behaviour of the resonance states whose energy lies near the localization point, in particular this mechanism is responsible of the binding of the resonance for large enough magnetic field [16], we will be back to this point in Section 4.

The similarities between the behaviour of the spectrum analyzed in Figure 1 near the point where $E_1^v \sim E_{\mathrm{LL}}(0, 0)$, and the spectrum of a two-electron quantum dot near the ionization threshold are striking. So, it comes as no surprise that the resonance states of both models also show some similarities, as we will show later on.

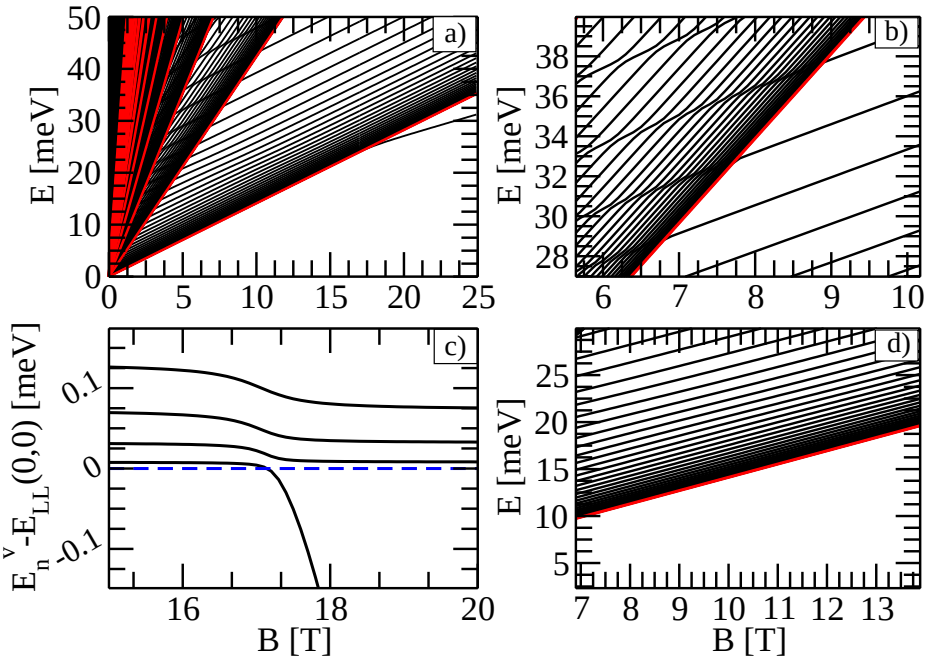

Figure 1. (Color on-line) The four panels show details of the variational spectrum and the Landau levels. a) The variational spectrum obtained with a basis set size $N = 2500$. Each black curve corresponds to a single eigenvalue and the red curves correspond to the exact Landau levels. b) This panel shows the zone around the second LL (red solid line). It can be seen how the levels that cross above the second LL have several avoided crossings before they reach the third one. c) This panel shows the difference between the lowest variational eigenvalues,E_n^v, and the first LL , $E_{\rm LL}(0,0)$, *vs.* the magnetic field, for $n = 1, \ldots, 4$. When the difference is smaller than zero, E_1^v crosses the first LL as can also be appreciated in panel a) besides, when $E_1^v < E_{\rm LL}(0,0)$ the corresponding eigenstate becomes localized. d) The eigenvalues above the first LL. The figure shows clearly how the eigenvalues are, basically parallel to the LL and accumulate above it.

3. Detecting the resonance states using complex exterior scaling

The calculation of the energy and width of resonance states offers a number of challenges that repeatedly leads to the formulation of new methods. Among the most widely used methods can be mentioned the complex scaling (or complex dilation) method [17], the complex absorbing potential method [27] and the density of states method [28]. Each one of these has its advantages and drawbacks. Because we are dealing with a piecewise potential we resort to the exterior complex scaling (see, for example, Reference [17]). This method is particularly appealing in our case since for $B \neq 0$, the complex scaling should be applied only to the z variable because this is the only direction available to the electron to get away from the bounding potential. The *exterior* of the method refers to the exterior of the region where the potential is not zero so, for $B \neq 0$ the exterior complex scaling asks that

$$z \longmapsto \begin{cases} z' & \text{if} \quad |z| \leq \frac{a_z + b_z}{2}, \\ e^{i\theta} z' & \text{if} \quad |z| \geq \frac{a_z + b_z}{2} \end{cases} , \tag{10}$$

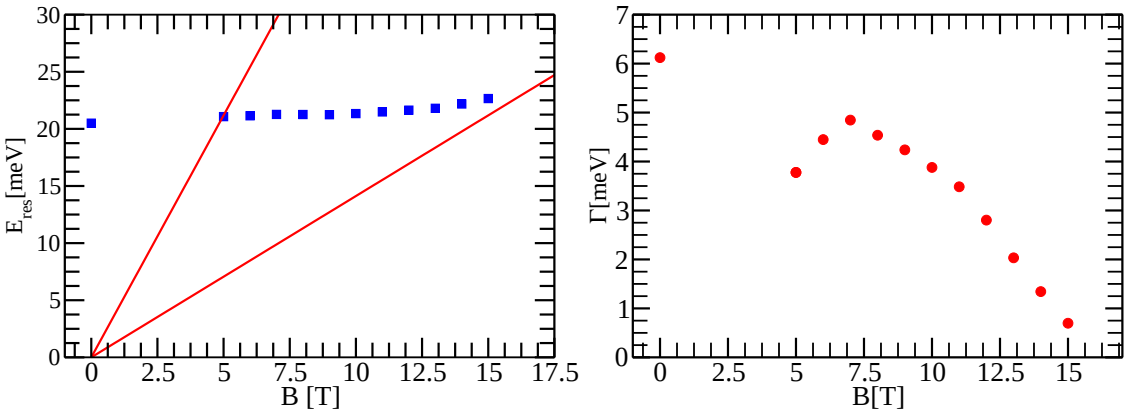

Figure 2. The real and imaginary parts of the resonance eigenvalue $E(\theta)$ *vs* the magnetic field strength. a) The solid square (blue) dots correspond to the energy of the resonance and the solid lines correspond to the two lowest Landau level energies. The value for $B = 0$ was obtained performing the complex rotation in the coordinates ρ and z. b) The width of the resonance *vs* the magnetic field. As the magnetic field increases its value the width of the resonance goes to zero, signaling its binding.

where z is the coordinate to be complex scaled, and θ is the rotation angle. The complex scaling turns the resonance states into normalizable states (with a different norm) which can be analyzed with the variational approach usually employed in Hermitian problems, *i.e.* the energy and width of the resonance state can be obtained approximately as an isolated complex eigenvalue of a finite (complex) Hamiltonian, if $H(\theta)$ is the complex scaled Hamiltonian, then we get a complex variational eigenvalue problem

$$\tilde{\mathbf{H}}(\theta)\mathbf{d}^{(j)} = E_j^v(\theta)\mathbf{d}^{(j)}, \tag{11}$$

where the entries of the matrix $\tilde{\mathbf{H}}(\theta)$ are given by

$$\tilde{\mathbf{H}}_{k,n,l,m}(\theta) = \langle \psi_k \phi_n | H(\theta) | \psi_l \phi_m \rangle \, . \tag{12}$$

Another advantage of the complex scaling method is given by the similarities between the matrix elements in Equation 12 with the ones calculated in Equation 9.

Figure 2 shows the behaviour of the energy and width of the lowest resonance as a function of the magnetic field strength. The binding of the resonance can be clearly observed, *i.e.* the width of the resonance drops to zero when the magnetic field strength increases its value. To obtain the data shown in Figure 2a) and b) we looked for the best value obtainable from the method, the complex rotation was performed for different values of θ and the best approximation corresponds to the stationary points of the θ-trajectory [17].

The exterior complex scaling methods works nicely for intermediate values of the magnetic field. Anyway, if $B \leq 5$T, or $B \geq 16$T, the convergence of the method is, at least, questionable, see Figure 3. For small fields the method struggles to provide a reliable value for the resonance eigenvalue because, as can be appreciated from Figure 2, for $B \approx 5$T the resonance "enters" in the continuum above the second Landau level (LL).

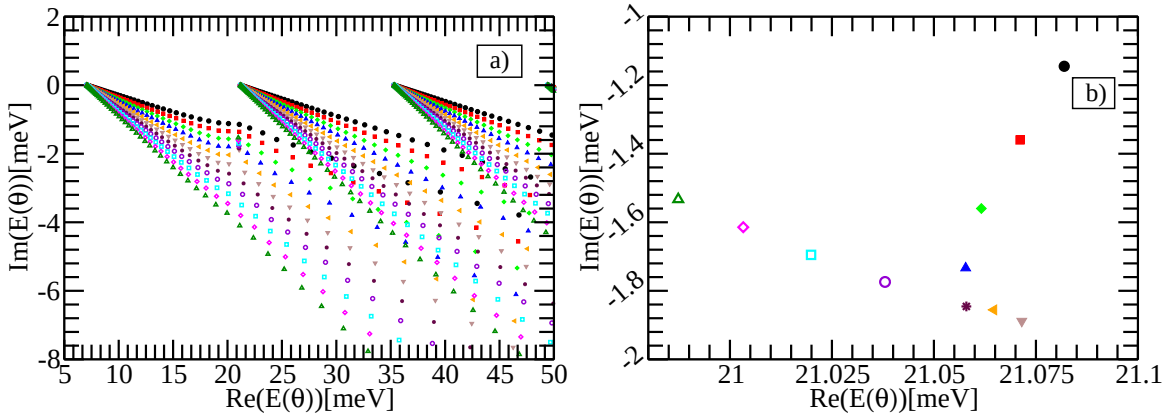

Figure 3. (Color on-line) a) The imaginary part *vs* the real part of the complex rotation eigenvalues . All the eigenvalues were calculated for $B = 5T$ and different rotation angles. From top to bottom, the eigenvalues correspond to $\theta = 0.1$ (black ●), $\theta = 0.11$ (red ■), $\theta = 0.12$ (green ♦), up to $\theta = 0.2$. The three fan-like sets of data are related to the first three LL's. Is is clear that the the leftmost fan and the central one start to overlap around 27 meV. For $B < 5T$ the overlap grows larger making more difficult to look for the resonance data. b) The θ trajectory of the resonance eigenvalue. The symbols correspond to the angles shown in panel a). The eigenvalues that form the θ trajectory can also be observed in panel a), they lie near the bump that presents the leftmost fan around 2 meV

In this region the approximate eigenvalues that enter from the region above the first Landau level "collide" with the eigenvalues that lie between the first and second LL. The successive collisions, and the corresponding avoided crossings, can be well appreciated in Figure 1b).

The binding of the resonance, *i.e.* that the width of the resonance becomes zero for large enough field strengths can not be understood only studying the spectrum. In the next Section, we will introduce a quantity that will allows us to study the associated eigenstates. As we will show, the analysis of the eigenstate corresponding to the isolated eigenvalue that appears below the first LL, see Figure 1a), gives a physical picture of the binding process.

In what follows, and up to the end of this Section, we want to focus in the results of the complex rotation method between Landau levels. The scenario between LL's can be better appreciated in Figure 3. The Figure shows the complex spectrum obtained when the complex rotation is performed accordingly with Equation 10 for different values of θ. In this Figure it is clear why the method is termed complex rotation, the continuum part of the spectrum now lies in the complex plane over straight lines, the angle between the lines and the real axis equal to 2θ. When $B \neq 0$, the data for different θ's form "hand-fans" of data, *i.e.* sets of straight lines with a common origin in the real axis. Each one of these sets can be associated to a single LL, the leftmost hand-fan corresponds to first LL, the middle one to the second LL, and the rightmost to the third LL. Again, this structure can be attributed to role that each LL plays as the bottom of

a continuum of levels. Effectively, the distance between the origins of each set of lines, over the real axis, is exactly equal to the distance between the LL at the magnetic field strength considered. As the magnetic field strength decreases, the data of the different fans overlaps making very difficult to distinguish the eigenvalues corresponding to the resonance.

Figure 3b) shows the trajectory in the complex plane of the eigenvalue associated to the resonance state. As can be appreciated, the eigenvalues are much less scattered in energy than in width. This feature is typical of the complex rotation method.

Above the second LL the complex rotation method should be complemented with some *ad hoc* assumptions to identify the points that belong to the θ-trajectory. The main assumption is rather physical: the complex rotated eigenvalues can be approximated by $E_{LL} + \tan(2\theta)\, E_n$, *i.e.* they form a straight line in the complex plane that form an angle of 2θ with the x-axis, E_n is a variational eigenvalue. This approximation works nicely **except** near a resonance. The second assumption is similar: a given complex eigenvalue $E_\nu(\theta)$ should not change too much if θ is changed, say

$$|E_\nu(\theta + \delta\theta) - E_\nu(\theta)| \leq \delta\theta |E_\nu(\theta)|, \tag{13}$$

where $\delta\theta$ is small enough. Applying these assumptions and discarding complex eigenvalues that jump from a hand-fan to another (see Figure 3a)) it is feasible to obtain stabilized values for E_{res} above the second LL.

4. Detecting the resonance states using Localization Probability

As we will show in this Section, the binding of the resonance for large enough magnetic field is a consequence of the strong localization experienced by the wave function corresponding to the lowest eigenvalue. As a matter of fact, the localization allows to follow the resonance through the spectrum. To quantify the localization of an approximate eigenfunction Ψ_j^v, we calculate the probability that the electron is localized in the potential well,

$$P_j = \int_{-\frac{a_z}{2}}^{\frac{a_z}{2}} \int_0^{a_\rho} \left|\Psi_j^v(\rho, z)\right|^2 \, d\rho \, dz \, , \tag{14}$$

where P_j is the probability attributable to the localization of Ψ_j^v.

Figure 4a) shows the probability P_1 as a function of the magnetic field strength for the lowest variational eigenvalue, while Figure 4b) shows the probability P_j for $j = 2, 3, \ldots, 8$. The curves are shown in different panels because of their respective scale.

It is worth to mention that despite the variational eigenvalues do not show any sudden changes near $B \sim 17$T, except for the lowest one when it crosses the first LL, the probability of localization into the well shows a well defined maximum for a large number of eigenvalues.

For small values of the magnetic field, the probability of localization $P_1 \lesssim 10^{-3}$ and is a very smooth function of B. This behaviour changes abruptly near $B \sim 17\,\mathrm{T}$, and

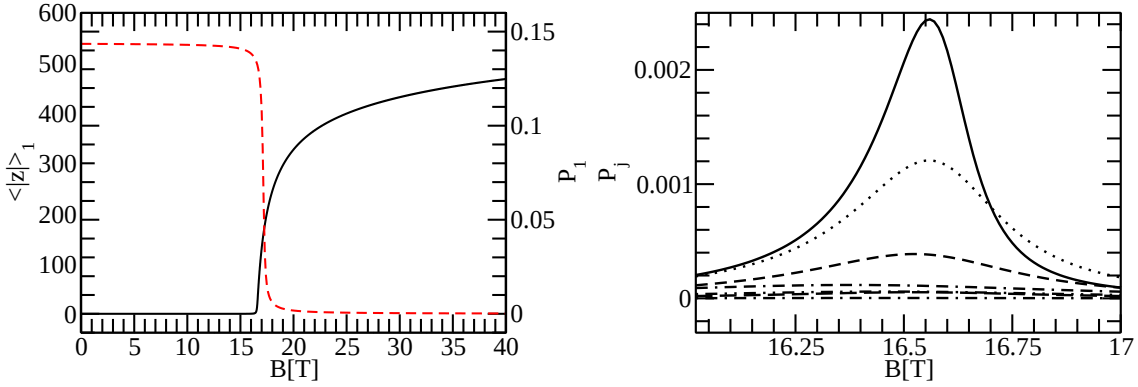

Figure 4. The localization probability *vs* the magnetic field strength. The left panel shows P_1 (black solid line), *i.e.* the probability corresponding to the lowest variational eigenvalue, and $\langle|z|\rangle_1$ (red dashed line). The scale of the right ordinate axis corresponds to P_1, while the scale of the left one corresponds to $\langle|z|\rangle_1$. The right panels shows, from top to bottom, P_2 (solid line), P_3 (dotted-line), ..., P_8. The localization probabilities show a peak where the corresponding eigenvalue crosses near the resonance, after and before the peak the eigenstate is extended.

for larger values of B the localization probability grows up to values larger than 0.1, see Figure 4a). It is clear that this behaviour is not compatible with an extended wave function. Since we are approximating the exact solutions of the eigenvalue problem with square-integrable functions, the value of the localization probability can not drop to zero, in the continuum region and far away from a resonance state, the variational eigenfunctions resemble a plane wave that is extended in a cylindrical spatial region with radius $R \sim 1/\eta$ and length $L \sim 1/\nu$, where η and ν are the non-linear variational parameters. For this reason, in the continuum region and far away from a resonance, we estimate the localization probability as $P_1 \sim a_z a_\rho \eta\nu \sim 10^{-3}$.

The localization of Ψ_1^v and can be further analyzed using the expectation value

$$\langle|z|\rangle_1 = \int_{-\frac{a_z}{2}}^{\frac{a_z}{2}} \int_0^{a_\rho} |\Psi_1^v(\rho, z)|^2 \, |z| d\rho \, dz \, , \tag{15}$$

where $|z|$ is the absolute value of z. Consistently with the behaviour observed for the localization probability, the expectation value $\langle|z|\rangle_1$ is very large for $B < 17\,\mathrm{T}$ and drops its value around two orders of magnitude for $B > 17\,\mathrm{T}$, see Figure 4a). We conclude that the wave function of the lowest variational eigenvalue becomes bounded. For the example that we are analyzing, $\langle|z|\rangle_1 \sim 540$ nanometers, for $B = 0$, and drops to $\langle|z|\rangle_1 \sim 3$ nanometers for $B \sim 18\,\mathrm{T}$. This last value is consistent with the longitudinal dimension of the quantum dot. Besides, as shown in Figure 1a), the lowest eigenvalue is isolated from the continuum for $B > 17\,\mathrm{T}$.

The scenario depicted above leads us to the following conclusion, the resonance above the first LL is triggered by the "collision" of the bounded state, corresponding to the lowest eigenvalue, with the continuum above the first LL. The avoided crossings originated by this collision can be clearly appreciated in Figure 1c), and reinforces the

interpretation that the binding of the resonance is produced when a bounded state appears for large enough magnetic field. In this sense, the resonance state behaves as a shape resonance and the radial potential owed to the magnetic field is the one changing its shape. The crossing of the lowest eigenvalue with the first LL corresponds, obviously, to the continuum threshold. Finally, as is the case in shape resonances, when the lowest eigenvalue is bounded and isolated the resonance width is zero, which explains the binding of the resonance for large enough fields.

The behaviour of the localization probabilities P_j, with $j > 1$ is quite different. These P_j are not monotonically increasing functions of B in contradistinction with P_1, instead they shown a more or less pronounced maximum for some value of B, see Figure 4b). The height of the maximum of a given P_j depends on the sharpness of the avoided crossing experienced by the corresponding eigenvalue. Sharper avoided crossings lead to higher maxima, smoother ones lead to lower maxima. This is consistent with the numerical spectrum obtained, since the avoided crossing of a low lying eigenvalue is always sharper than the avoided crossing of a higher eigenvalue.

We interpret that the peak in a given localization probability appears when the corresponding eigenvalue is a reasonable approximation for the resonance energy at that particular value of B. In other words, $E_{res}(B_j^{peak}) \approx E_j^v(B_j^{peak})$, where B_j^{peak} is the value of the magnetic field where P_j attains its maximum. The $E_j^v(B_j^{peak})$ allow to track down the resonance states from the localization point up to the second LL, above the second LL the spectrum shows a multiple-continua region, generating multiple avoided crossings due to two-continua interaction that this method can not distinguish from the avoided crossings due to resonances. The $E_j^v(B_j^{peak})$ are shown in Figure 7, where they are compared to the resonance energies obtained using the other methods discussed in this work.

5. Detecting the resonance states using the Fidelity

For a given quantum state ψ, that depends on a parameter λ, a measure of how much it changes when the parameter is varied is given by the fidelity, $\mathcal{F}$, which is defined as

$$\mathcal{F}_{\Delta\lambda}(\lambda) = |\langle\psi(\lambda - \Delta\lambda), \psi(\lambda + \Delta\lambda)\rangle|^2 , \tag{16}$$

where $\Delta\lambda$ is a small variation of the parameter.

The fidelity has been extensively used to characterize the analytical properties of quantum states near a quantum phase transition in quantum spin chains models [29], quantum phases of matter [30],or bound and resonance states in atomic or quantum dot models [18]. In two-electron quantum dots, it has been shown that the fidelity of the approximate variational eigenstates detect the resonance states and allow to calculate approximately its energy [18]. To achieve this, the fidelity of many eigenstates should be calculated as a function of the external parameter that drives the system from bound to unbounded states. In this work, this parameter is the magnetic field strength.

From its definition, Equation 16, it is clear that most of the time $\mathcal{F}_{\Delta\lambda} \approx 1$, except for very special cases. On the other hand the fidelity should drop to zero if the system

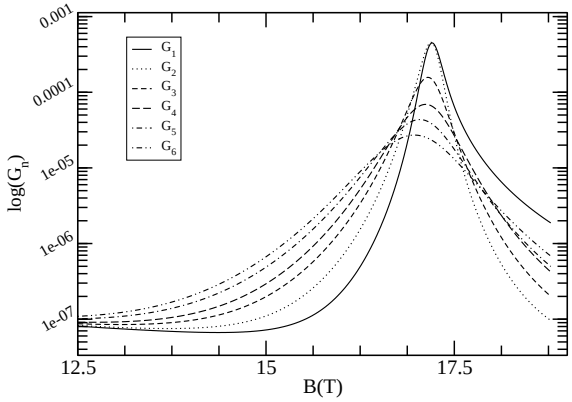

Figure 5. The function $\mathcal{G}_n$ *vs* the magnetic field. The figure shows the function for the first six variational eigenvalues, $\mathcal{G}_1$, $\mathcal{G}_2$, ..., $\mathcal{G}_6$, solid (——), dotted (· · · · · ·), short-dashed (- - - -), long-dashed (— — —), dot-dashed (— · —) and double dot-dashed (— · · —) lines respectively. The peak where each curve attains its maximum value is clearly appreciable. B_n is given by the abscissa of the peak (see the text).

experiments a rather sudden change [29]. For this reason, often it is convenient to study the function

$$\mathcal{G}_n(\lambda) = 1 - \left|\langle \Psi_n^v(\lambda - \Delta\lambda), \Psi_n^v(\lambda + \Delta\lambda)\rangle\right|^2 . \tag{17}$$

Figure 5 shows the behaviour of the $\mathcal{G}_n$ function for $n = 1, 2, \ldots, 6$, as function of the magnetic field strength. Each curve has a more or less well defined peak for a given value of the magnetic field, B_n. The values $E_n(B_n)$, *i.e.* the value of the variational eigenvalues at their respective peaks of the function $\mathcal{G}_n$, give a very good approximation for the resonance energy at the points B_n. This way to obtain a estimation for the resonance energy does not allow to obtain it for arbitrary magnetic field strength values since the values B_n are not chosen at will, they are obtained from the fidelity data and depend on the basis set size, the non-linear variational parameters, the basis functions used, and so on, this has been pointed out previously in Reference [18]. Nevertheless the method provides another tool to analyze resonance states. The fidelity method works best when the width of the resonance is not too wide, so it is to be expected that it will be more precise near the localization point.

Before presenting the results of the localization and fidelity methods with respect to the resonant states, we want to stress the relationship between both quantities. Let us call $B_p(a_\rho)$ the critical value of the magnetic field such that the localization probability of the first variational eigenvalue becomes noticeable for a given quantum dot radius a_ρ, and $B_{\mathcal{F}}(a_\rho)$ the magnetic field value such that the function $\mathcal{G}_1$ attains its maximum value as a function of B. Figure 6 shows the values of both quantities, $B_p(a_\rho)$ and $B_{\mathcal{F}}(a_\rho)$, for several values of the quantum dot radius a_ρ. The agreement between both critical quantities is striking.

At this point, we can summarize our results in Figure 7. The Figure shows the energy of the resonant state as a function of B, as it is obtained from the complex

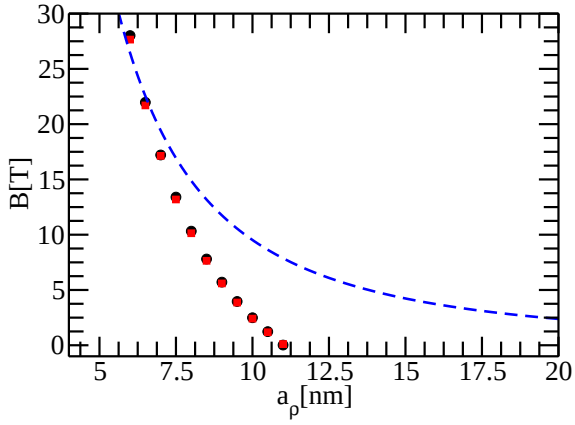

Figure 6. (Color on-line) The critical fields $B_p(a_\rho)$ and $B_{\mathcal{F}}(a_\rho)$ *vs* the quantum dot radius. The localization probability critical field (red squared dots, ■) and the fidelity critical field (solid black dots, ●) data is shown for several quantum dot radius. The (blue) dashed curve correspond to the radius of the lowest LL as a function of the magnetic field. It is clear that for small quantum dot radius the localization takes place when the cylindrical wave function enters into the cylindrical QD. For larger QD's radius the localization is dominated by the quantum well potential and not by the magnetic field.

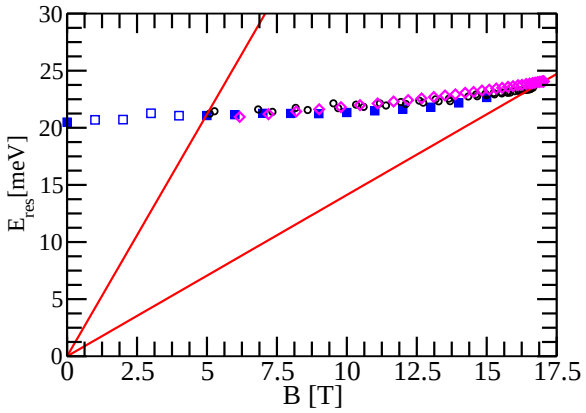

Figure 7. The resonance energy E_{res} calculated using the three methods depicted in the text, complex exterior scaling, localization probability, fidelity, the corresponding values are shown using blue square dots (■), black circles (○), and magenta diamonds (♢). The energy of the resonance in the region above the second LL can be obtained using a modified version of the complex rotation method and is shown using blue open squares (□) .

rotation, fidelity and localization methods.

From Figure 7 is rather clear that both the localization method and the fidelity are able to follow the resonance from the localization point until the second Landau level. Anyway, a word of caution is necessary here. The complex rotation method implies a stabilization procedure that, when properly used, gives an idea about the accuracy of the results obtained. This is not true for the Fidelity method. The best recipe to obtain

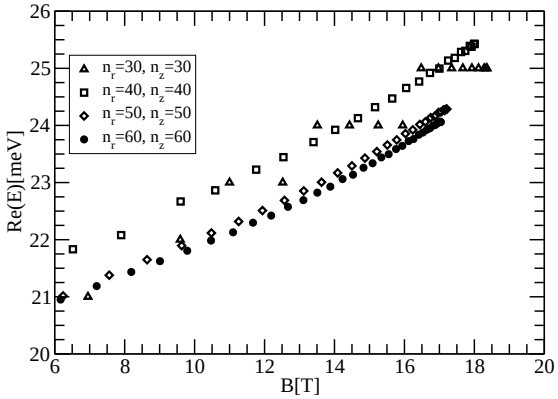

Figure 8. $E_n(B_n)$ *vs* the magnetic field strength. The figure shows the data obtained using different basis set sizes, $N = 30 \times 30$, triangle up open dots; $N = 40 \times 40$, square open dots; $N = 50 \times 50$, diamond open dots; and $N = 60 \times 60$, solid dots.

stabilized results from the Fidelity method implies picking the largest possible basis set size, N, with $N_z = N_\rho$. Otherwise, the convergence of the Fidelity data, *i.e* the values obtained for the resonance's energy from the Fidelity, is not uniform. Figure 8 shows the behaviour of the resonance energy obtained following the Fidelity method with different basis set sizes. It is worth to mention that the resonance energies obtained with $N = 900$ and $N = 3600$ differ in less than 5%

Again, as is the case with the localization probability method to find estimations for the resonance energy, the fidelity method works properly as long as the resonance state is well isolated, *i.e.* the only avoided crossings present in a given region of the spectrum should be one associated to the resonance. As has been said previously, above the second LL there is a very large number of avoided-crossings for each eigenvalue. owed to a multiple-continua scenario. Each $\mathcal{G}_n$ has a peak associated to every single avoided-crossing, making extremely hard to decide which peak corresponds to the resonance state.

6. Discussion and Conclusions

The external magnetic field precludes the escape of the electron on the (ρ, ϕ) plane, for this reason the quantum dot bounding potential consists of a potential well and a potential step, to ensure the presence of resonance states. In this sense, the problem has several characteristic lengths, the quantum dot radius, the Landau levels radii, the length of the quantum dot along the z axis, and so on. The two lengths that come into play varying the magnetic field strength, for the set of parameters considered in this work, are the quantum dot radius and the lowest LL radius. The potential well depth and the other parameters of the QD were chosen to ensure that for $B = 0$ there were no bound states.

The localization probability is able to track down the resonance states from the

localization point up to the second LL. Above the second LL the eigenvalues have too many avoided crossings, because of the multiple-continua interacting in this region of the spectrum, rendering the method useless. The many avoided crossings also prevent the use of the fidelity to detect the resonance above the second LL. Moreover, despite that the width of the resonance state analyzed is not small when compared with the resonance energy, the fidelity method provides a good estimation of the last. Anyway, some precaution must be exercised to obtain accurate and stable results.

Finally, both critical fields, $B_p(a_\rho)$ and $B_{\mathcal{F}}(a_\rho)$, show two clearly distinguishable regimes, for small quantum dot radius their values are given by the lowest Landau level radius, so both are proportional to $1/a_\rho^2$. For large enough quantum dot radius both critical fields show a different behaviour and, apparently, both are proportional to $(\alpha - \beta a_\rho)^2$, where α y β are constants. The extent of the small field regime can be tuned changing the parameters of the bounding potential, Equation 1, extending or reducing it. The critical behaviour of the eigenvalues in the transition region between the large field-small quantum dot radius and the small field-large quantum dot radius will be analyzed elsewhere.

Acknowledgments

We would like to acknowledge SECYT-UNC, CONICET, and MinCyT Córdoba for partial financial support of this project. We would like to thank Dr. Pablo Serra for helpful comments and the critical reading of this manuscript.

Appendix A. Some matrix elements

It is convenient to separate the kinetic energy matrix elements in two contributions, one corresponding to the radial coordinate,

$$\begin{aligned}\langle \psi_n \left| T_\rho \right| \psi_s \rangle &= \left\langle \psi_n \left| -\frac{1}{2\mu}\nabla_r^2 \right| \psi_s \right\rangle \\ &= \frac{\eta}{\mu\sqrt{(n+1)(s+1)}}\left(\frac{1}{4}T_1 + \frac{1}{2}\left(T_2+T_3\right)+T_4\right)\end{aligned} \tag{A.1}$$

and the other corresponding to the z coordinate,

$$\begin{aligned}\langle \phi_t \left| T_z \right| \phi_r \rangle &= \left\langle \phi_t \left| -\frac{1}{2\mu}\nabla_z^2 \right| \phi_r \right\rangle \\ &= \frac{\eta}{2\mu\sqrt{(n+1)(s+1)}}\left(\frac{1}{4}T_{1z} + \frac{1}{2}\left(T_{2z}+T_{3z}\right)+T_{4z}\right)\end{aligned} \tag{A.2}$$

where

$$\begin{aligned}T_1 &= (n+1)\delta_{n,s}, \\ T_2 &= \sum_{p=0}^{n}\sum_{q=0}^{s-1}\frac{(-1)^{p+q}(n+1)!(s+1)!(p+q+1)!}{(n-1-p)!(2+p)!p!(s-q)!(1+q)!q!},\end{aligned} \tag{A.3}$$

$$T_3 = \sum_{p=0}^{n-1}\sum_{q=0}^{s} \frac{(-1)^{p+q}(n+1)!(s+1)!(p+q+1)!}{(n-p)!(1+p)!p!(s-1-q)!(2+q)!q!},$$
$$T_4 = \sum_{p=0}^{n-1}\sum_{q=0}^{s-1} \frac{(-1)^{p+q}(n+1)!(s+1)!(p+q+1)!}{(n-1-p)!(2+p)!p!(s-1-q)!(2+q)!q!} \tag{A.4}$$

while

$$T_{1z} = \delta_{t,r},$$
$$T_{2z} = \sum_{d=0}^{t}\sum_{f=0}^{r-1} \frac{(-1)^{t+r}t!\ r!(d+f)!}{(t-d)!(d!)^2(r-1-f)!(1+f)!f!}, \tag{A.5}$$
$$T_{3z} = \sum_{d=0}^{t-1}\sum_{f=0}^{r} \frac{(-1)^{t+r}t!\ r!(d+f)!}{(t-1-d)!(1+d)!(r-f)!(f!)^2},$$
$$T_{4z} = \sum_{d=0}^{t-1}\sum_{f=0}^{r-1} \frac{(-1)^{t+r}t!\ r!(d+f)!}{(t-1-d)!(1+d)!d!(r-1-f)!(1+f)!f!}. \tag{A.6}$$
$$\tag{A.7}$$

The matrix element of the bounding potential can be factorized owed to its piecewise character and using that there is a potential barrier on the z direction. We get that

$$\langle \psi_n \phi_t \left| V(\rho, z) \right| \psi_s \phi_r \rangle = -V_2\, I_{V2} + V_1\, I_{V1} \delta_{n,s}, \tag{A.8}$$

the barrier term is, obviously, proportional to V_1, while the term proportional to V_2 corresponds to the matrix element of the potential well. The matrix elements I_{V2} and I_{V1} are given by

$$I_{V2} = \frac{1}{\sqrt{(n+1)(s+1)}} \sum_{p=0}^{n}\sum_{q=0}^{s} \frac{(-1)^{p+q}(n+1)!(s+1)!\ I_{V21}}{(n-p)!(1+p)!p!(s-q)!(1+q)!q!}$$
$$\times \sum_{d=0}^{t}\sum_{f=0}^{r} \frac{(-1)^{d+f}t!\ r!\ I_{V22}}{(t-d)!(d!)^2(r-f)!(f!)^2} \tag{A.9}$$
$$I_{V1} = \frac{1}{\sqrt{(n+1)(s+1)}} \sum_{d=0}^{t}\sum_{f=0}^{r} \frac{(-1)^{d+r}t!\ r!\ I_{V11}}{(t-d)!(t!)^2(r-f)!(f!)^2} \tag{A.10}$$

and

$$I_{V21} = (p+q+1)! - e^{-\eta a} \sum_{k=0}^{p+q+1} \frac{(p+q+1)!(a\eta)^{p+q+1-k}}{(p+q+1-k)}, \tag{A.11}$$
$$I_{V22} = (d+f)! - e^{-\nu a/2} \sum_{g=0}^{d+f} \frac{(d+f)!}{(d+f-g)} \left(\frac{\nu a}{2}\right)^{d+f-g}, \tag{A.12}$$

$$I_{V11} = \sum_{k=0}^{d+f} \frac{(d+f)!}{(d+f-k)!}$$

$$\times \left(e^{-a\nu/2} \left(\frac{a\nu}{2}\right)^{d+f-k} - e^{\frac{-(a+b)\nu}{2}} \left(\frac{(a+b)\nu}{2}\right)^{d+f-k} \right). \tag{A.13}$$

The matrix element of the magnetic field term reads as

$$\begin{aligned} \langle \psi_n \left| H_c \right| \psi_s \rangle \; &= \frac{B^2}{8\mu\eta^2\sqrt{(n+1)(s+1)}} \\ &\times \sum_{p=0}^{n} \sum_{q=0}^{s} \frac{(-1)^{p+q}(n+1)!(s+1)!(p+q+3)!}{(n-p)!(1+p)!p!(s-q)!(1+q)!q!} \end{aligned} \tag{A.14}$$

[1] Bayer M, Korkusinski M, Hawrylak P, Gutbrod T, Michel M, and Forchel A 2003 *Phys. Rev. Lett.* **90** 186801

[2] Mailly D, Chapelier C and Benoit A 1993 *Phys. Rev. Lett.* **70** 2020

[3] Kleemans N, Bominaar-Silkens I, Fomin V, Gladilin V, Granados D, Taboada A, García A, Offermans P, Zeitler U, Christianen P, Maan J, Devreese J and Koenraad P 2007 *Phys. Rev. Lett.* **99** 146808

[4] Somaschini C, Bietti S, Koguchi N and Sanguinetti S 2009 *Nano Letters* **9** 3419

[5] Sikorski Ch and Merkt U 1989 Phys. Rev. Lett **62** 2164

[6] Peeters F M 1990 *Phys. Rev. B* **42** 1486

[7] Geerinckx F, Peeters F M and Devreese J T 1990 *J. Appl. Phys.* **68** 3435

[8] Peeters F M and Schweigert V A 1996 *Phys. Rev. B* **53** 1468

[9] Partoens B, Matulis A and Peeters F M *Phys. Rev. B* **59** 1617

[10] Loss D and DiVincenzo D 1998 *Phys. Rev.* A **57** 120

[11] Takahashi R, Kono K, Tarucha S and Ono K 2011 *Phys. Rev. Lett.* **107** 026602

[12] Petta R, Johnson A, Taylor J, Laird E, Yacoby A, Lukin M, Marcus C, Hanson M and Gossard A 2005 *Science* **309** 2180

[13] Kwasniowski A and Adamowski J 2009 *J. Phys: Condens. Matter* **21** 235601

[14] Szafran B, Peeters F and Bednarek S 2004 *Phys. Rev.* B **70** 125310

[15] Zhang L, Melnikov D, Agarwal S and Leburton J 2008 *Phys. Rev.* B **78** 035418

[16] Bylicki M and Jaskólski W 1999 *Phys. Rev.* B **60** 15924

[17] Moiseyev N 1998 *Phys. Rep.* **302** 211

[18] Pont F, Osenda O, Toloza J and Serra P 2010 *Phys. Rev.* A **81** 042518

[19] Ferrón A, Osenda O and Serra P 2009 *Phys. Rev.* A **79** 032509

[20] Nazmitdinov R, Simonović N, Plastino A and Chizhov A 2012 *J. Phys. A: Math. Theor.* **45** 205503

[21] Abdullah S, Coe J and DAmico I 2009 *Phys. Rev.* B **80** 235302

[22] Osenda O and Serra P 2007 *Phys. Rev.* A **75** 042331

[23] Majtey A, Plastino A and Dehesa J 2012 *J. Phys. A: Math. Theor.* **45** 115309

[24] Bylicki M, Jaskólski W, Stachów A and Diaz J 2005 *Phys. Rev.* B **72** 075434

[25] A T Kruppa and K Arai, Phys. Rev. A **59**, 3556 (1999)

[26] Bylicki M 2008 *J. Phys.: Conf. Ser.* **104** 012022

[27] Sajeev Y, Vysotskiy V, Cederbaum L and Moiseyev N 2009 *J. Chem. Phys.* **131** 211102

[28] Mandelshtam V A, Ravuri T R and Taylor H S 1993 *Phys. Rev. Lett.* **70** 1932

[29] Zanardi P and Paunković N 2006 Phys. Rev E **74** 031123

[30] Garnerone S, Abasto D, Haas S and Zanardi P 2009 *Phys. Rev.* A **79** 032302